Infant Brain Extraction in T1-weighted MR Images using BET and Refinement using LCDG and MGRF Models

Amir Alansary*, *Member, IEEE*, Marwa Ismail*, Ahmed Soliman, *Member, IEEE*, Fahmi Khalifa, *Member, IEEE*, Matthew Nitzken, *Member, IEEE*, Ahmed Elnakib, *Member, IEEE*, Mahmoud Mostapha, *Member, IEEE*, Austin Black, Katie Stinebruner, Manuel F. Casanova, Jacek M. Zurada, *Life Fellow, IEEE,* and Ayman El-Baz*, *Member, IEEE*

Abstract*—In this paper, we propose a novel framework for the automated extraction of the brain from T1-weighted MR images. The proposed approach is primarily based on the integration of a stochastic model (a two-level Markov-Gibbs random field (MGRF)) that serves to learn the visual appearance of the brain texture, and a geometric model (the brain iso-surfaces) that preserves the brain geometry during the extraction process. The proposed framework consists of three main steps: (*i*) Following bias correction of the brain, a new 3D MGRF having a 26-pairwise interaction model is applied to enhance the homogeneity of MR images and preserve the 3D edges between different brain tissues; (*ii*) The non-brain tissue found in the MR images is initially removed using the brain extraction tool (BET), and then the brain is parceled to nested iso-surfaces using a fast marching level set method; (*iii*) Finally, a classification step is applied in order to accurately remove the remaining parts of the skull without distorting the brain geometry. The classification of each voxel found on the iso-surfaces is made based on the first- and second-order visual appearance features. The first-order visual appearance is estimated using a linear combination of discrete Gaussians (LCDG) to model the intensity distribution of the brain signals. The second-order visual appearance is constructed by using a MGRF model with analytically estimated parameters. The fusion of the LCDG and MGRF, along with their analytical estimation, allows the approach to be fast and accurate for use in clinical applications. The proposed approach was tested on *in-vivo* data using 300 infant 3D MR brain scans which were qualitatively validated by an MR expert. In addition, it was quantitatively validated using 30 data sets based on three metrics: the Dice coefficient, the 95-percentile modified Hausdorff distance, and absolute brain volume difference. Results show the capability of the proposed approach, outperforming four widely used brain extraction tools: BET, BET2, brain surface extractor (BSE), and infant brain extraction and analysis toolbox (iBEAT). Experiments conducted also proved that the proposed framework can be generalized to adult brain extraction as well.

***Index Terms*—Infant Brain, Skull Stripping, MRI, LCDG, MGRF, BET, Iso-surfaces.**

Amir Alansary, Marwa Ismail, Ahmed Soliman, Matthew Nitzken, Fahmi Khalifa, and Ahmed Elnakib are with the BioImaging Laboratory, Bioengineering Department, University of Louisville, Louisville, KY 40292, USA.

Manuel F. Casanova is with the Department of of Psychiatry and Behavioral Science, University of Louisville, Louisville, KY, USA.

Jacek M. Zurada is also with the Spoleczna Akademia Nauk, 90-011 Lodz, Poland.

* indicates shared first authorship

*Ayman El-Baz is with the BioImaging Laboratory, Bioengineering Department, University of Louisville, Louisville, KY 40292, USA (Corresponding author, e-mail: aselba01@exchange.louisville.edu).

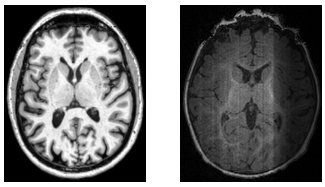

(a) (b)

Fig. 1. T1-weighted MRI scans for adult (a) and infant (b) brains.

I. Introduction

BRAIN extraction is the process of removing all the outer tissues (e.g. eyes, dura, scalp, and skull) around the brain, which consists of the gray matter (GM) and white matter (WM), while the inclusion of cerebrospinal fluid (CSF) in the brain depends on the application. Brain extraction is a primary step in neuroimaging analysis as well as a pre-processing step for many brain analysis algorithms like intensity normalization, registration, classification, and segmentation. Accordingly, accurate brain extraction is crucial for these algorithms to work properly. For instance, in cortical thickness estimation, inaccurate skull stripping (e.g. failing to remove the dura or missing brain parts) can result in an overestimation or underestimation of the cortical thickness [1].

Extraction of brains from adult scans is a difficult process, yet is more challenging in the case of infants due to many factors including the difference in size of the corresponding anatomy, and the variability in the properties of the signal acquired. This explains the fact that most of the work in literature is devoted to brain extraction from adult scans, and that fewer techniques are focused on infant brain extraction.

Many brain extraction approaches have been developed to extract the brain from T1-weighted MR brain images. These methods use different techniques, such as, region growing, deformable models, atlas-based and label fusion, and hybrid algorithms. Park et al. [2] automatically identified two seed points of the brain and non-brain regions using morphological operations. Then 2D region growing was employed based on knowledge of brain anatomy. This was extended by Roura et al. [3], where a Multispectral Adaptive Region Growing Algorithm (MARGA) was proposed. This enabled the use of [2] to axial views and provided more reliable

results for different patient populations and different MRI scanners (1.5 T and 3 T). Smith [4] developed an automated deformable model-based method, which is widely known as the brain extraction tool (BET). In their approach, the deformable contour is guided by a set of locally adaptive forces, which include morphological and image-based terms in addition to a surface smoothness constraint. Liu et al. [5] presented another deformable model-based brain extraction method using a set of Wendland's radial basis functions [6]. Their deformable model is directed by an internal force to consider the smoothness constraint and an external force to impose the intensity contrast across the boundaries. Finally, the brain contours are constructed by integrating the 2D coronal and sagittal slices that were separately computed to obtain a complete 3D brain volume. Also, Zhuang et al. [7] used a level set-based deformable model that combines two forces: the mean curvature of the curve and the intensity characteristics of the cortex in MR images. Baillard et al. [8] developed a deformable model-based approach to find the brain surface. As an alternative solution for initializing the first contour manually, an atlas-based technique is used to make the brain extraction process entirely automatic. After atlas registration and initial segmentation, the brain is finally segmented based on level sets with adaptive parameters depending on the input data. Wang et al. [9] used an atlas-based approach for skull-stripping, along with a deformable-surface-based approach guided by local intensity information and prior information that is learned from a set of real brain images. Sadananthan et al. [10] presented a skull stripping approach using graph cuts, which consists of two steps. An initial brain mask is generated using intensity thresholding as a first step. Then, a graph theoretic image segmentation method is applied to position cuts which remove narrow connections. Zhaung et al. [11] developed a method for brain extraction by estimating image intensity parameters to construct a binary image of the head. Then, an initial contour is estimated. The final brain is extracted using an improved geometric active contour model which extends the solution of the boundary leakage problem to make it insusceptible to the inhomogeneity of intensity. Somasundaram et al. [12] developed a contour-based method to segment the brain from T1-, T2-, and proton density weighted MRI of human head scans in 2 phases. The first phase involves extraction of brain regions in the middle slice, with a landmark circle drawn at the center of the extracted brain region. The second phase extracts brain regions in the rest of the slices with reference to that landmark circle. Leung et al. [13] presented a brain extraction technique using a template library. Multiple best-matched atlases are selected by comparing the target image to all the atlases in that library. In order to segment the target image optimally after image registration, label fusion techniques do the task of combining the labels from all atlases incorporated. Iglesias et al. [14] developed a learning-based brain extraction algorithm that has two models: a discriminative model based on a random forest classifier trained to detect the brain boundary, and a generative model based on finding the contour with highest likelihood according to the discriminative model, which is refined later using graph cuts. Segonne et al. [15] presented a hybrid approach that combines watershed algorithms and deformable surface models. The watershed, with a preflooding height, construct an initial estimate of the brain volume using a single white matter voxel as a global minimum. Then, a surface deformation process is used to correct the initial segmentation inaccuracies. A statistical atlas is used finally to potentially correct the segmentation. Beare et al. [16] introduced marker-based watershed scalper (MBWSS) for brain extraction in T1-weighted MR images that is built using filtering and segmentation components from the Insight Toolkit (ITK) framework. Rex et al. [17] developed a meta-algorithm that uses four freely available brain extraction algorithms: brain surface extractor (BSE) [18], brain extraction tool (BET) [4], 3dIntracranial [19], and MRI watershed from FreeSurfer [20]. For extracting the brain, an atlas is used to define which extraction algorithm or combination of extractors works best defining the brain in each anatomic region.

As mentioned earlier, there has not been much work in literature addressing infant brain extraction. To the best of our knowledge, we are briefly presenting all the existing techniques. Chiverton et al. [21], for example, used parameter estimation to fit a Gaussian model to a predefined histogram. The extraction process then employed 3D morphological operators. Another approach was proposed by Kobashi et al. [22], where connected triangles were used in order to construct an initial surface model, to be deformed by moving the vertices. Fuzzy rules were used to define the positions of the triangles. Peporte et al. [23] Presented an approach called Hybrid Skull-Stripping (HSS). A binary mask was generated using morphological operators to define the brain tissue outer boundary, which was later followed by region growing and edge detection. In order to improve the accuracy, a unique threshold value was identified for each slice in the volume using k-means clustering. In [24], multiple brain extractions using BET and BSE are applied on test subjects, where the parameters of each technique are learned from the training data. Also, the representative subjects are selected as exemplars and used to guide brain extraction of new subjects in different age groups. A level-set based fusion method was further used to combine the multiple brain extractions in order to get the final result.

In summary, different brain extraction approaches have been developed; however, they have their own drawbacks. Some of them give better results when removing non-brain tissue while losing some brain parts, and others give better results when extracting the whole brain while keeping some non-brain tissue parts [25], [26]. Atlas-based approaches are very time consuming and their performance heavily depends on the registration accuracy between the atlas and the test subject, in addition to the difficulty of constructing an infant brain atlas [27]. Moreover, the majority of the existing techniques are developed to work for adult MR brain images and fail to accurately extract the brain from MR infant images due to the reduced contrast and higher noise [28]. The infant brain MRI extraction meets with challenges stemming from image noise, inhomogeneities, artifacts, and discontinuities of boundaries arising from similar visual appearance of adjacent brain structures, see Fig. I. Furthermore, accurate infant brain extraction contributes much to the analysis, treatment, and the

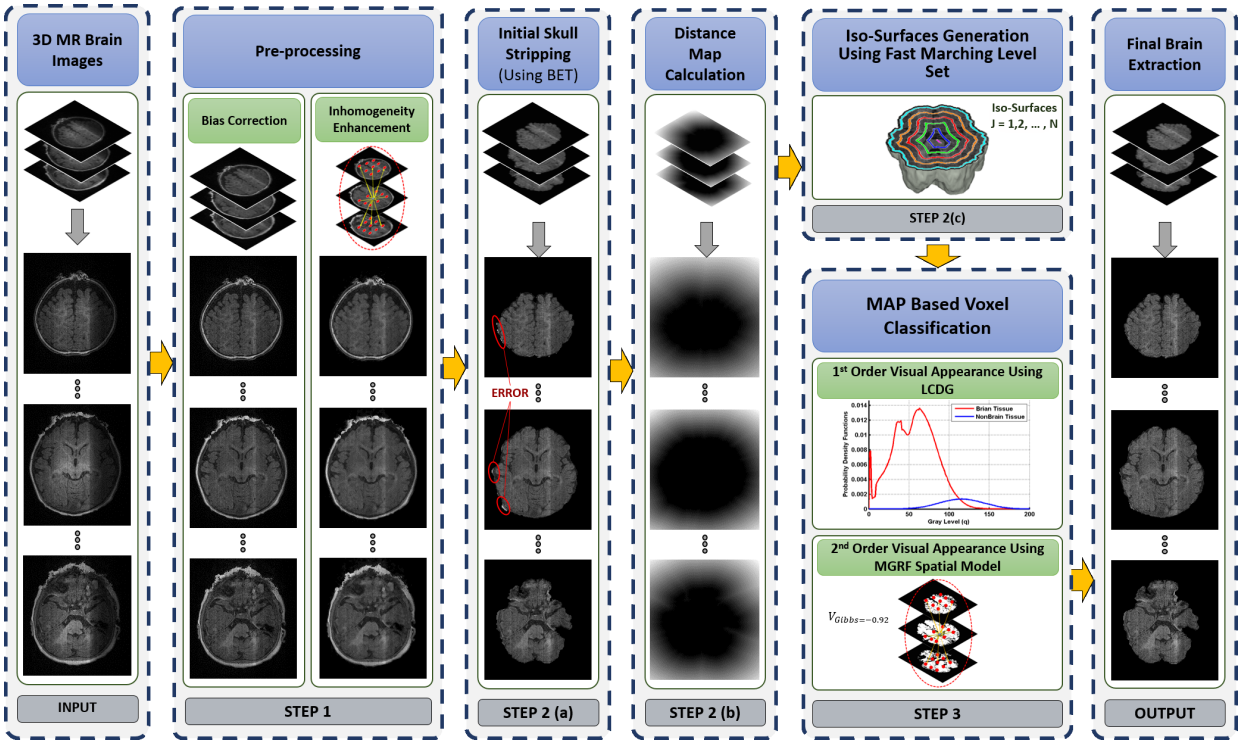

Fig. 2. The basic steps of the proposed framework for brain extraction from infant MR brain data.

early diagnosis of brain injury and disorders resulting from the infant prematurity.

II. Methods

To overcome the aforementioned limitations, we present a hybrid framework, shown in Fig. 2, that possesses the ability to accurately extract brain tissue from infant MR brain images. The proposed framework integrates both stochastic and geometric approaches and consists of three basic steps: (*i*) bias correction and inhomogeneity enhancement, (*ii*) Initial skull stripping and iso-surfaces generation, and (*iii*) final brain extraction using the visual appearance features of the MR brain images. The proposed approach avoids many of the shortcomings of the methods presented in literature. One of the main advantages of it is that it does not require shape priors. Moreover, it is not atlas-based, and thus its accuracy is not affected by any related processes such as registration. Also the integration of geometric features guarantees retaining all brain parts. Inaccurate skull stripping can drastically affect subsequent processes such as shape analysis for diagnosis of Autism [29]. The proposed approach aims at handling all sources of such inaccuracies. Details of the proposed approach are outlined in the following sections.

A. Bias Correction and Inhomogeneity Enhancement

Illumination non-uniformity of infant brain MRIs, which is known as bias field, limits the accuracy of the existing brain extraction approaches. Therefore, to accurately extract the brain it is important to account for the low frequency intensity non-uniformity or inhomogeneity. In this work, we use a 3D generalized Gauss-Markov random field (GGMRF) model [30] that is applied after bias correction of the brain using the nonparametric approach proposed in [31]. This step reduces noise effects and removes (smooth) inconsistencies of the MRI data by accounting for the 3D spatially homogeneous pair-wise interactions between the gray levels of the MRI data. Namely, the gray level values $q \in \mathbf{Q} = \{0, \ldots, Q-1\}$ are considered as samples from a 3D GGMRF model [30] represented for the 26-neighborhood of a voxel. The maximum A posteriori (MAP) estimates [30] and voxel-wise stochastic relaxation (iterative conditional mode (ICM) [32]) of q values of each brain MR scan are employed as follows:

$$\widehat{q}_s = \arg\min_{\widetilde{q}_s} \left[|q_s - \widetilde{q}_s|^{\alpha} + \rho^{\alpha} \lambda^{\beta} \sum_{r \in \nu_s} \eta_{s,r} \, |\widetilde{q}_s - q_r|^{\beta} \right] \quad (1)$$

where q_s and $\widetilde{q}_s$ are the original gray level values and their expected estimates, respectively, at the observed 3D location, $s = (x, y, z)$; ν_s is the 26-neighborhood system; $\eta_{s,r}$ is the GGMRF potential, and ρ and λ are scaling factors. The parameter $\beta \in [1.01, 2.0]$ controls the level of smoothing (e.g., $\beta = 2$ for smooth vs. $\beta = 1.01$ for relatively abrupt edges). The parameter $\alpha \in \{1, 2\}$ determines the Gaussian, $\alpha = 2$, or Laplace, $\alpha = 1$, prior distribution of the estimator. Fig. 2, Step 1 demonstrates the effect of pre-processing of our framework.

B. Initial Skull Stripping and Iso-surfaces Generation

The second step of the proposed framework is to initially remove the non-brain tissue from the MR images. To accomplish this, we used the BET [4] which is a widely used deformable model-based approach for stripping the skull from brain MRIs. The process of skull stripping is very sensitive to

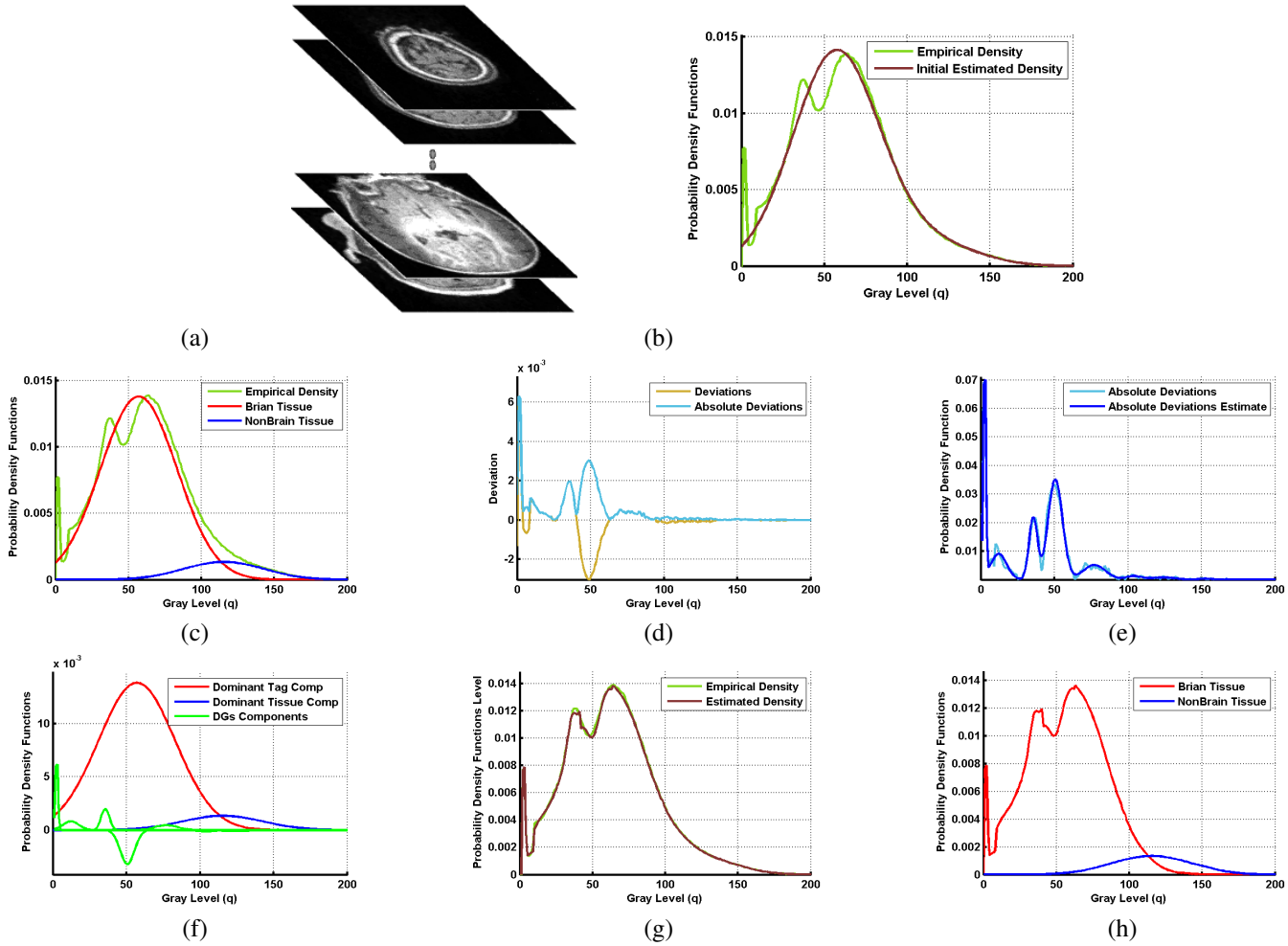

Fig. 3. Typical MR infant brain images (a); and estimated density (b) using only two dominant Gaussian components (c), deviation between empirical and estimated densities (d), estimated density of absolute deviation (e), LCDG components (f), final estimated density (g), and the final estimated marginal density for each class (h).

the assigned BET factor. Using a high value would result in removing most of the undesired non-brain tissues, yet losing details of the brain tissues. On the other hand, a lower BET factor would preserve most of the brain tissues as well as non-brain tissues. The BET factor used for best results was 0.38. Fig. 2, Step 2 (a) demonstrates the idea. While the BET extracted the brain without losing any of its parts using the assigned BET factor, it failed to remove all non-brain tissues. For some clinical applications, such as cortical thickness measurement, inaccurate skull stripping results in an over- or under-estimation of the thickness. This can drastically affect further analysis, such as feature extraction needed for detection of abnormalities. Therefore, it is important to account for inaccurate skull stripping results after the BET step. In order to improve the result obtained from BET, we propose an additional processing step based on the geometric features of the brain to account for BET's skull stripping errors. Since the non-brain tissues are brighter than brain tissue, this step exploits the visual appearance features of the MR brain data. Namely, an evolving iso-surface-based approach is proposed to remove the non-brain tissues, which is guided by the visual appearance features of the MR data (see Fig. 2, Steps 2 (b), 2 (c)). First, a set of nested, tangent surfaces (i.e., iso-surfaces) are generated by the fast marching level set (FMLS) approach [33], using the calculated distance map of the extracted brain from the BET step. Then classification of voxels as brain or non-brain is conducted and is presented in the following section.

C. *Modeling Visual Appearance Using 3D joint MGRF*

In order to classify MRI voxels as brain or non-brain, we need to accurately model MR data visual appearance. To achieve this goal, we will use a 3D joint Markov-Gibbs random field (MGRF) model, which is described as follows:

Let $\mathbf{Q} = \{0, \ldots, Q-1\}$ and $\mathbf{L} = \{\text{"brain"}, \text{"non-brain"}\}$ denote sets of gray levels q and region labels L, respectively. Let $\mathbf{R}$ denote a 3D arithmetic lattice supporting a given grayscale image $\mathbf{g} : \mathbf{R} \rightarrow \mathbf{Q}$ and its region map $\mathbf{m} : \mathbf{R} \rightarrow \mathbf{L}$. The 3D T1-weighted MR images, $\mathbf{g}$, and its map, $\mathbf{m}$, are described with the following joint probability model:

$$P(\mathbf{g}, \mathbf{m}) = P(\mathbf{g}|\mathbf{m})P(\mathbf{m}) \quad (2)$$

where $P(\mathbf{m})$ is an unconditional probability distribution of maps, and $P(\mathbf{g}|\mathbf{m})$ is a conditional distribution of the images

given the map. The ultimate goal is to accurately estimate $P(\mathbf{g}|\mathbf{m})$ and $P(\mathbf{m})$, which are described next.

1) First-order visual appearance $P(\mathbf{g}|\mathbf{m})$: To accurately approximate the marginal probability distributions of the brain and non-brain tissue, the empirical gray level distribution of a given brain data is precisely approximated with a linear combination of discrete Gaussians (LCDG) with positive and negative components [34]. The LCDG restores brain and non-brain transitions more accurately than a conventional mixture of only positive Gaussians. This results in obtaining a better initial map $\mathbf{m}$ formed by voxel-wise classification of the image gray values. Next the LCDG is explained in more details.

Let $\mathbf{\Psi}_\theta = (\psi(q|\theta) : q \in \mathbf{Q})$ define a discrete Gaussian (DG)[1] where $\theta = (\mu, \sigma)$, integrating a continuous 1D Gaussian density with mean μ and variance σ^2 over successive gray level intervals [34]. The LCDG with two dominant positive DGs and $M_{\rm p} \geq 2$ positive and $M_{\rm n} \geq 0$ negative subordinate DGs is defined as [34]:

$$P_{\mathbf{w},\mathbf{\Theta}}(q) = \sum_{i=1}^{M_{\rm p}} w_{{\rm p}:i}\psi(q|\theta_{{\rm p}:i}) - \sum_{j=1}^{M_{\rm n}} w_{{\rm n}:j}\psi(q|\theta_{{\rm n}:j}) \quad (3)$$

where all the weights $\mathbf{w} = [w_{{\rm p}:i}, w_{{\rm n}:j}]$ are non-negative and meet an obvious constraint $\sum_{i=1}^{M_{\rm p}} w_{{\rm p}:i} - \sum_{j=1}^{M_{\rm n}} w_{{\rm n}:j} = 1$. All the LCDG parameters, including the numbers of DGs, are estimated from the mixed empirical distribution to be modeled using the modified expectation-maximization (EM)-based algorithm introduced in [35].

The marginal intensity distributions of the MR infant images have two dominant modes: one mode for brain tissues and a second mode for non-brain tissues. Figure 3 shows the steps to build the LCDG models of the two modes. First, the marginal empirical probability distribution of the input grey level images (Fig. 3 (a)) are collected (Fig. 3 (b)). Then, the obtained empirical distribution is approximated with a mixture of two positive DGs relating each to a dominant mode (Fig. 3 (c)). Second, the deviations between the empirical and the estimated distribution (Fig. 3 (d)) are approximated with the alternating "subordinate" components of the LCDG described in [35]. Finally, the obtained positive and negative subordinate mixtures (Fig. 3 (f)) are added to the dominant mixture yielding the final mixed LCDG model (Fig. 3 (g)), which is partitioned into two LCDG-submodels (one per class, Fig. 3 (h)) by incorporating the subordinate DGs with the dominant terms so that the misclassification rate obtained is minimal [34].

2) 3D Second-order visual appearance ($P(\mathbf{m})$): In order to overcome noise effect and to ensure segmentation homogeneity, the spatial interactions between the region labels of a brain map $\mathbf{m}$ are also considered using Potts MGRF model. This model is identified using the nearest voxels' 26-neighbors (as shown in Fig. (4 (a))) and analytical bi-valued Gibbs potentials (as shown in Fig. (4 (b))). The 3D MGRF model is defined by [36] as:

$$P(\mathbf{m}) \propto \exp \sum_{(x,y,z)\in\mathbf{R}} \sum_{(\xi,\zeta,\kappa)\in\nu_s} \mathbf{V}(m_{x,y,z}, m_{x+\xi,y+\zeta,z+\kappa}) \quad (4)$$

where $\mathbf{V}$ is the bi-value Gibbs potential, that depends on the equality of the nearest pair of labels:

$$V = \begin{cases} V(\lambda,\lambda') = V_{\rm eq} & \text{if} \quad \lambda = \lambda' \\ V(\lambda,\lambda') = V_{\rm ne} & \text{if} \quad \lambda \neq \lambda' \end{cases} \quad (5)$$

Let $f_{a,{\rm eq}}(\mathbf{m})$ denote the relative frequency of the equal label pairs in the equivalent voxel pairs $\{((x,y,z),(x+\xi,y+\zeta,z+\kappa)) : (x,y,z),(x+\xi,y+\zeta,z+\kappa) \in \mathbf{R}; (\xi,\zeta,\kappa) \in \nu_s\}$. The initial $\mathbf{m}$ results in approximate analytical maximum likelihood potentials estimates [36]:

$$V_{\rm eq} = -V_{\rm ne} \approx 2f_{\rm eq}(\mathbf{m}) - 1 \quad (6)$$

that allow for computing the voxel-wise probabilities $p_{x,y,z}(m_{x,y,z} = \lambda)$ of each label $\lambda \in \mathbf{L}$. Fig. 2, Step 3 shows the classification process. Algorithm 1 summarizes the basic steps of the proposed framework.

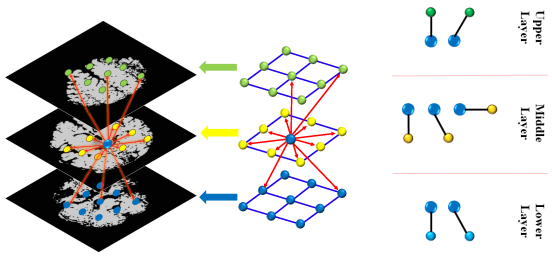

(a) (b)

Fig. 4. A graphical illustration for the 3D neighborhood system (a) and a sample of the different pair-wise cliques for the 2nd-order MGRF (b).

III. Performance Evaluation Metrics

The performance of the proposed framework was evaluated using three performance metrics: (*i*) the Dice similarity coefficient (DSC) [37], (*ii*) the 95-percentile modified Hausdorff distance (MHD) [38], and (*iii*) the absolute brain volume difference (ABVD). The following subsections explain the three metrics in more detail.

A. Dice similarity coefficient (DSC)

The dice similarity coefficient (DSC) characterizes the agreement between the segmented and ground truth objects (as seen in Fig. 5). The DSC measure is given from [37] as:

$$DSC = \frac{2TP}{2TP + FP + FN} \quad (7)$$

where TP, FP, and FN denote the true positive, false positive, and false negative respectively. Higher DSC values indicate better segmentation, which means that the results match the ground truth better than results with lower DSC values. A DSC value of 0 indicates no overlap and a DSC value of 1 indicates ideal segmentation (or agreement).

[1]A Discrete Gaussian (DG) $\Psi_\theta = (\psi(q|\theta) : q \in \mathbf{Q})$ with $\theta = (\mu, \sigma^2)$ is defined as $\psi(q|\theta) = \Phi_\theta(q + 0.5) - \Phi_\theta(q - 0.5)$ for $q = 1, \ldots, Q - 2$, $\psi(0|\theta) = \Phi_\theta(0.5)$, and $\psi(Q - 1|\theta) = 1 - \Phi_\theta(Q - 1.5)$ where $\Phi_\theta(q)$ is the cumulative Gaussian function with the mean μ and the variance σ^2.

Algorithm 1 Proposed Brain Extraction Approach

1) Perform pre-processing on the MR brain data:
   a) Bias correction of the brain [31].
   b) GGMRF edge preservation, Fig. 2, Step1.
2) Perform initial skull stripping using BET [4], Fig. 2, Step2 (a).
3) Calculate the distance map inside the binary mask obtained from BET using FMLS [33], then generate a set of N iso-surfaces from this map, Fig. 2, Step 2 (b),(c).
4) Estimate the LCDG models for brain and non-brain tissues and form an initial map $\mathbf{m}$ by voxel-wise classification, Fig. 2, Step 3.
5) Estimate analytically the Gibbs potentials for the pairwise MGRF model of $\mathbf{m}$ to identify the MGRF probability, Fig. 2, Step 3.
6) while $j \leq N$
   a) Select the j^{th} iso-surfacer and classify its voxels using a Bayes classifier combining the first and second-order visual appearance features.
   b) Are all the voxels on the selected iso-surfaces classified only as brain tissue?
      - No $\longrightarrow$ **Go to Step 6 (a)**.
      - Yes $\longrightarrow$ **Break**
7) Apply connected component analysis to get rid of any scattered non-brain tissues, Fig. 2, Step 4.

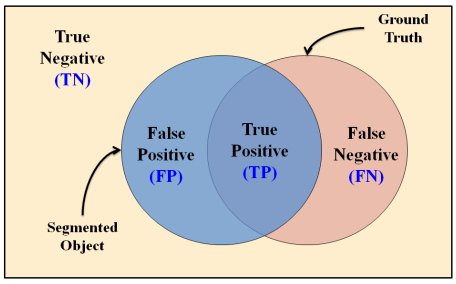

Fig. 5. Segmentation errors calculation between the segmented and ground truth objects for the determination of the dice similarity coefficient (DSC).

B. Modified Hausdorff distance (MHD)

In order to measure the error distance between the segmented and ground truth objects, we used the modified hausdorff distance (MHD). The Hausdorff distance (HD) [38] from a set A_1 to a set A_2 is defined as the maximum distance of the set A_1 to the nearest point in the set A_2 (as shown in Fig. 6):

$$H(A_1, A_1) = \max_{c \in A_1} \{ \min_{e \in A_2} \{ d(c, e) \} \} \tag{8}$$

where c and e denote points of set A_1 and A_2 respectively, and $d(c, e)$ is the Euclidean distance between c and e.

The bidirectional HD between the segmented region SR and its ground truth GT is defined as:

$$H_{Bi}(GT, SR) = max\{H(GT, SR), H(SR, GT)\} \tag{9}$$

In this paper, we use the 95th-perecntile biderictional HD as a metric that measures the segmentation accuracy, which is also known as the modified Hausdorrf Distance (MHD).

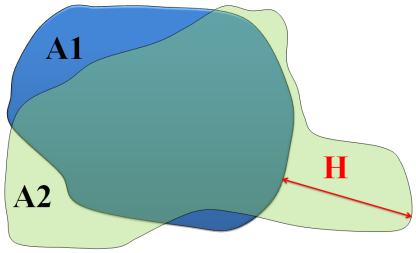

Fig. 6. A schematic illustration for the Haussdorf distance (HD) calculation.

C. Absolute brain volume difference (ABVD)

In addition to the DSC and the MHD, we have used the absolute brain volume difference (ABVD) as a third metric for measuring the segmentation accuracy. The ABVD is the percentage volume difference between the segmentation and the ground truth as seen in Fig. 7.

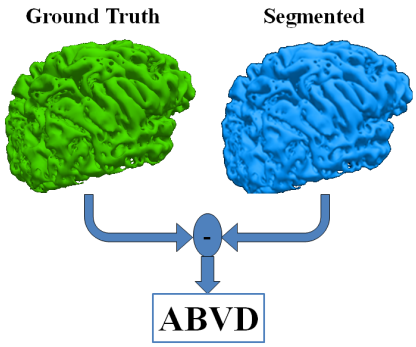

Fig. 7. 3D schematic illustration for the absolute brain volume difference (ABVD) estimation.

IV. Experimental Results

In order to assess the robustness and performance of the proposed framework, we applied it to 300 T1-weighted MR infant brain data sets which were obtained from the Infant Brain Imaging Study (IBIS) [39]. An MR expert assessed the results qualitatively. In addition, the accuracy of the proposed approach was quantitatively validated using 30 data sets with known manually segmented ground truth that were obtained by an MR expert. MR data was acquired at 3T and consists of T1- and T2-weighted MR images of infants scanned at approximately 5-9 months old with voxel size of $1 \times 1 \times 1$ mm^3.

A step-wise brain extraction using the proposed approach for a selected axial cross-section of one subject is demonstrated in Fig. 8. The input MR image (Fig. 8 (a)) is first bias corrected (Fig. 8 (b)) and applied to the 3D GGMRF [30] edge preservation (Fig. 8 (c)). This is followed by an initial brain extraction using BET [4] (Fig. 8 (d)). As mentioned in Section II, a relatively small BET factor was chosen in order to minimize the loss of brain tissues. The average value concluded from the experiments on the subjects used is 0.38. The proposed iso-surfaces based approach (Fig. 8 (e)) is then employed to achieve the final skull stripping as shown in Fig. 8 (f). It is clear from the results in Fig. 8 that the proposed framework provides more accurate infant brain extraction than

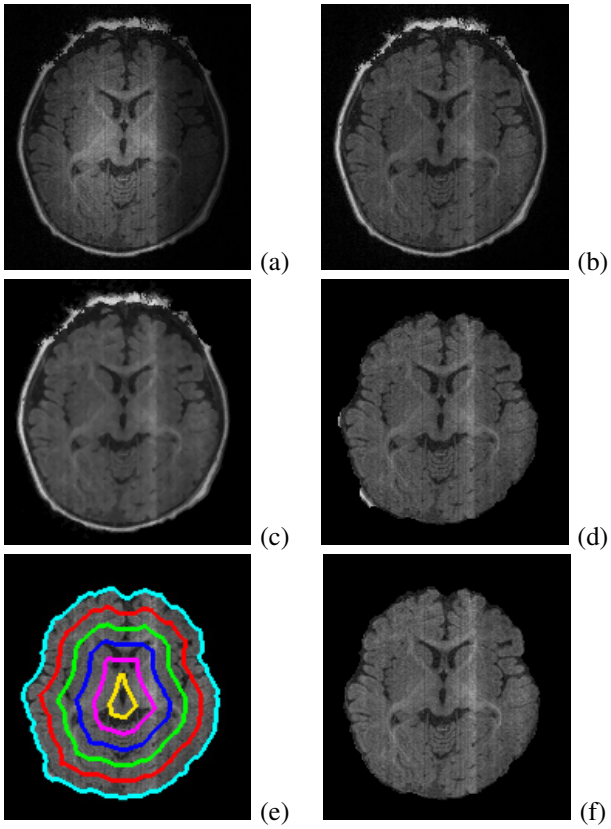

Fig. 8. Step-wise brain extraction using our framework: (a) the original MR image, (b) the bias-corrected image, (c) the GGMRF-edge preserved image obtained with $\rho = 1$, $\lambda = 5$, $\beta = 1.01$, $\alpha = 2$, and $\eta_{s,r} = \sqrt{2}$, (d) the extracted brain using BET [4], (e) the iso-surfaces used to remove non-brain tissues, and (f) the final extracted brain.

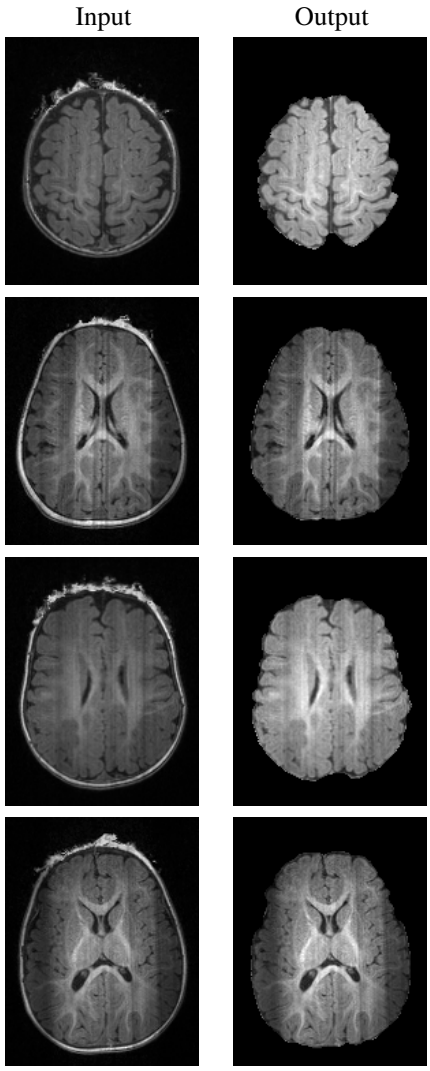

Fig. 9. More stripping results for different cross-sections from different subjects showing reliable brain extraction using the proposed approach.

BET. More stripping results for different cross-sections from different subjects are shown in Fig. 9.

To highlight the advantage of the proposed framework, we compared its performance to one of the state-of-the-art tools for infant brain extraction, called the infant brain extraction and analysis toolbox iBEAT [24]. The version used is iBEAT 1.1 which is a Linux-based software package, and is publicly available at http://www.nitrc.org/projects/ibeat. The iBEAT performs multiple complementary brain extractions using a meta-algorithm as mentioned in the introduction section, yet, Fig. 10 (images results) and Fig. 13 (a), (e) (volume results) show that the proposed approach provides more accurate stripping results. Also Table I shows that our approach performs notably better, according to the higher DSC and lower MHD values and ABVD values .

In addition to the comparison with iBEAT, we also compared our approach to three widely-used brain extraction tools for adult brain extraction: the brain surface extractor (BSE) [18], the brain extraction tool (BET) [4], and the BET2 [40]. This comparison was conducted to show that the existing approaches for adult brain extraction would have low accuracy on infant brains. The comparative accuracy of the proposed approach versus the BSE, BET, and BET2 techniques on representative images for 3 subjects is shown in Fig. 11. As demonstrated in Fig. 11 and the 3D extracted brains shown in Fig. 13, our approach extracted the brain tissue more accurately compared with the other approaches. The lower performance of the BET [4] could be caused by its sensitivity to image noise and inhomogeneity, because this method relies only on voxels' intensity changes and does not account for spatial voxel interactions. On the other hand, the BET2 approach [40] slightly improves the brain extraction accuracy compared with the BET one. However, unlike the BET and our approach, the BET2 technique requires both T1- and T2-weighted MR images. BSE [18] succeeds in accurately removing the skull but it removes parts from the brain tissues as well, which may lead to inaccurate results for some clinical application (e.g. cortical thickness under-estimation). Table I compares our approach with the, BSE, BET, and BET2, based on the DSC, MHD, and ABVD metrics. All metrics were obtained by comparing brain extraction results against the 30 data sets with available ground truth segmentation. As demonstrated in Table I, the mean DSC, MHD, and ABVD values for our framework are 96.77$\pm$1.45%, 4.14$\pm$1.76 mm, and 4.95$\pm$2.62%, respectively, which confirm the high accuracy of our approach. Statistical significance of the better performance of our approach with respect to other methods is confirmed by

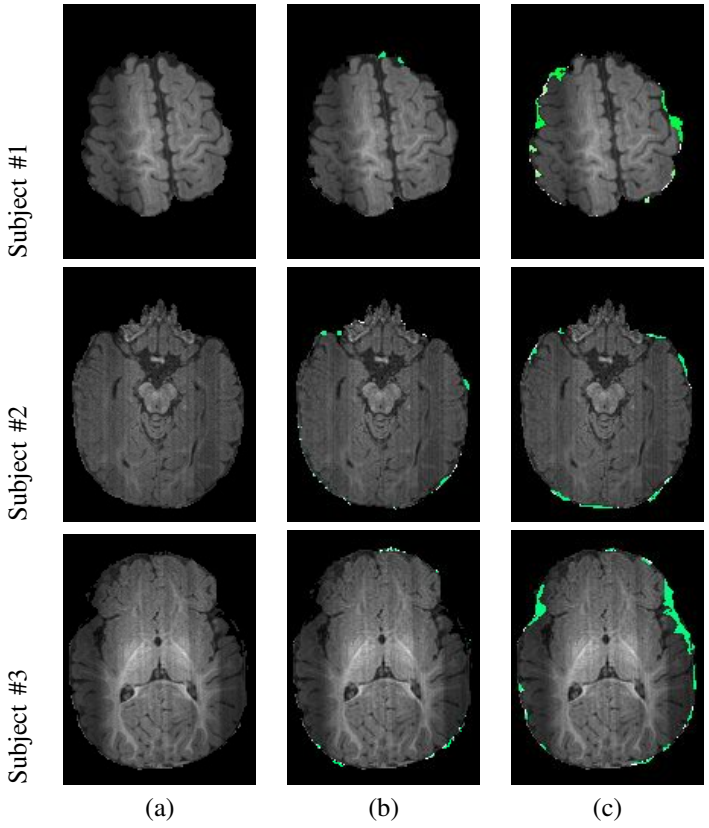

Fig. 10. Comparative infant brain extraction results for three independent subjects using (b) the proposed approach, and (c) iBEAT [24]. Ground truth images are shown in (a).

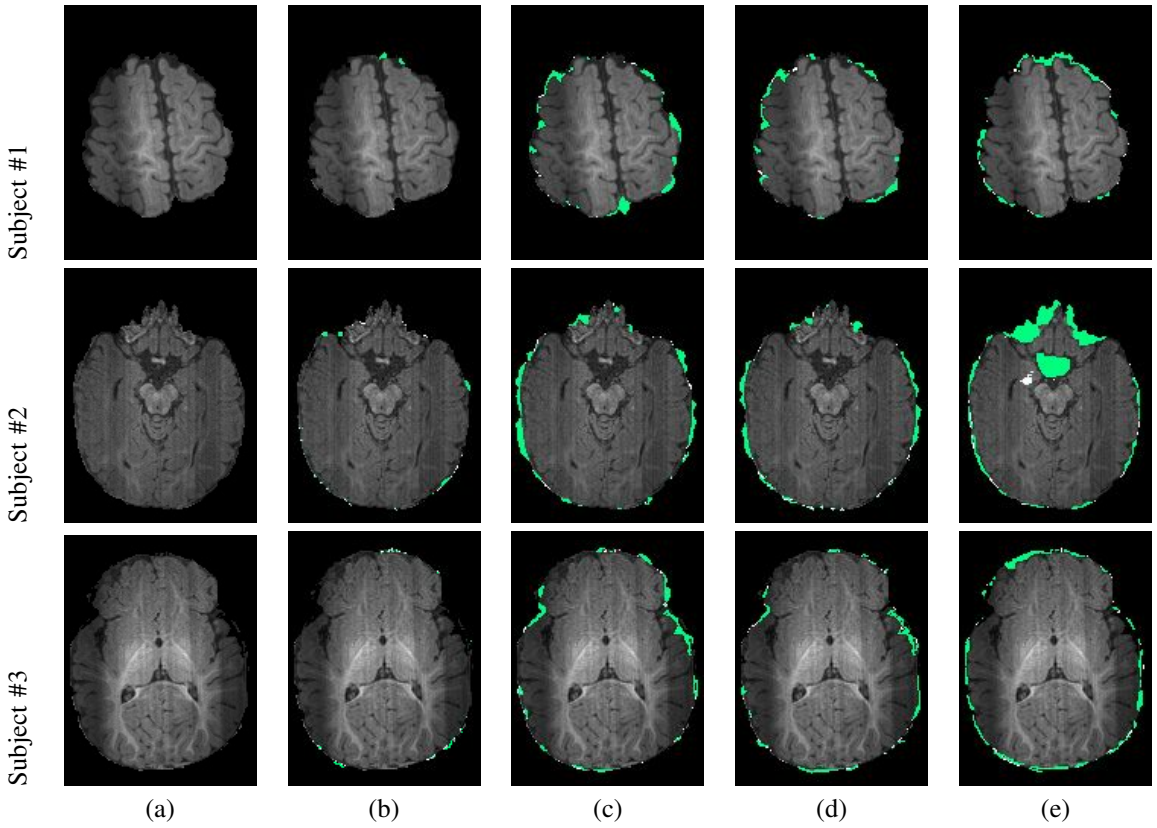

Fig. 11. Comparative infant brain extraction results for three independent subjects using (b) our approach, (c) BET [4], (d) BET2 [40], and (e) BSE [18]. Ground truth images are shown in (a).

the paired t-tests (p-values are less than 0.05). Fig. 12 shows more results of the proposed approach on 2 infant subjects tn the 3 views: axial, coronal, and sagittal.

In order to show that our approach is not limited to infants and that it could be generalized to adult brains, we applied it on 18 adult subjects and compared its performance to that of BSE, BET, and BET2. The scans are T1-weighted, with voxel size of 0.958mm x 0.958mm x 3.0mm. They have been acquired at the UMC Utrecht (the Netherlands) of patients with diabetes and matched controls with varying degrees of atrophy and white matter lesions, and ages are 50 and higher. The comparative accuracy of the proposed approach versus BSE, BET, and BET2 on representative images for 2 subjects is shown in Fig. 14. As demonstrated, our approach, Fig. 14 (b), extracted the brain tissue more accurately compared with the other approaches. Table II compares our approach on adults with the, BSE, BET, and BET2, based on the DSC, MHD, and ABVD metrics. All metrics were obtained by comparing results against the 18 data sets with available ground truth segmentation. As demonstrated in Table II, the mean DSC, MHD, and ABVD values for our framework are $93.11\pm2.4\%$, 8.43 ± 1.88 mm, and $6.7\pm1.13\%$, respectively.

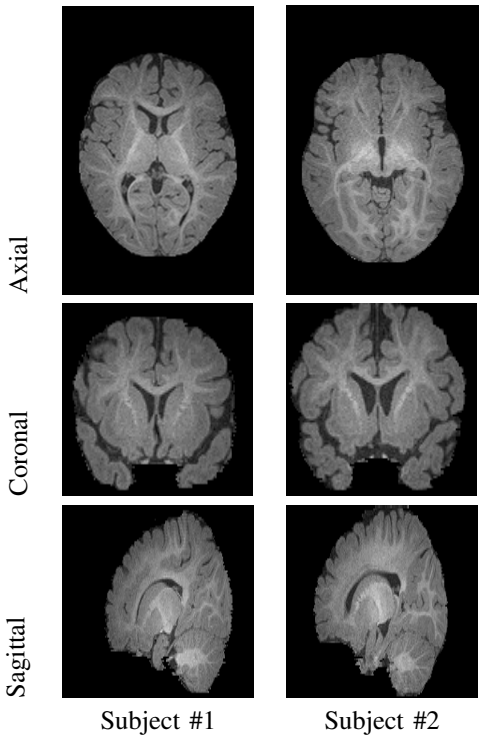

Fig. 12. Results of the proposed approach on two independent infant subjects, showing each of them in the axial, coronal, and sagittal views respectively.

V. Conclusions and Future Work

In conclusion, this paper has introduced a novel framework for automated extraction of the brain from 3D infant MR images. Our experiments show that the fusion of stochastic and geometric models of the brain MRI data leads to more accurate brain extraction, when compared with widely-used brain extraction tools: iBEAT, BSE, BET, and BET2. The results were evaluated using the DSC, 95-percentile MHD, and the ABVD metrics on 30 infant MR brain data sets. The proposed approach also proved efficient when applied on adult brains, and compared vs. state-of-the-art methods. A future extension of this work would be integrating the proposed skull stripping approach into a CAD system for early detection of Autism, which is the ultimate goal of our research group. Integrating higher-order cliques could be another extension to the proposed framework, where, currently, the 3D joint MGRF model with only pairwise cliques is exploited. Higher order cliques (e.g. third- and fourth-order) will better account for noise and large inhomogeneities of the MRI scans of infants.

References

[1] A. J. van der Kouwe, T. Benner, D. H. Salat, and B. Fischl, "Brain morphometry with multiecho mprage," *Neuroimage*, vol. 40, no. 2, pp. 559–569, 2008.

[2] J. G. Park and C. Lee, "Skull stripping based on region growing for magnetic resonance brain images," *NeuroImage*, vol. 47, no. 4, pp. 1394–1407, 2009.

[3] E. Roura, A. Oliver, M. Cabezas, J. C. Vilanova, A. Rovira, L. Rami-Torrent, and X. Llad, "Marga: Multispectral adaptive region growing algorithm for brain extraction on axial mri," *Computer methods and programs in biomedicine*, vol. 113, no. 2, pp. 655–673, 2014.

[4] S. M. Smith, "Fast robust automated brain extraction," *Human Brain Mapping*, vol. 17, no. 3, pp. 143–155, 2002.

[5] J.-X. Liu, Y.-S. Chen, and L.-F. Chen, "Accurate and robust extraction of brain regions using a deformable model based on radial basis functions," *Journal of Neuroscience Methods*, vol. 183, no. 2, pp. 255–266, 2009.

[6] H. Wendland, "Piecewise polynomial, positive definite and compactly supported radial functions of minimal degree," *Advances in computational Mathematics*, vol. 4, no. 1, pp. 389–396, 1995.

[7] A. H. Zhuang, D. J. Valentino, and A. W. Toga, "Skull-stripping magnetic resonance brain images using a model-based level set," *NeuroImage*, vol. 32, no. 1, pp. 79–92, 2006.

[8] C. Baillard, P. Hellier, and C. Barillot, "Segmentation of brain 3D MR images using level sets and dense registration," *Medical Image Analysis*, vol. 5, no. 3, pp. 185–194, 2001.

[9] Y. Wang, J. Nie, P. T. Yap, G. Li, F. Shi, X. Geng, L. Guo, and D. Shen, "Knowledge-guided robust mri brain extraction for diverse large-scale neuroimaging studies on humans and non-human primates," *Plos*, vol. 9, no. 1, 2014.

[10] S. A. Sadananthan, W. Zheng, M. W. Chee, and V. Zagorodnov, "Skull stripping using graph cuts," *NeuroImage*, vol. 49, no. 1, pp. 225–239, 2010.

[11] H. Zhang, J. Liu, Z. Zhu, and H. Li, "An automated and simple method for brain MR image extraction," *Biomedical Engineering Online*, vol. 10, no. 1, p. 81, 2011.

[12] K. Somasundaram and P. Kalavathi, "Contour-based brain segmentation method for magnetic resonance imaging human head scans," *Journal of computer assisted tomography*, vol. 37, no. 3, pp. 353–368, 2013.

[13] K. K. Leung, J. Barnes, M. Modat, G. R. Ridgway, J. W. Bartlett, N. C. Fox, and S. Ourselin, "Brain MAPS: an automated, accurate and robust brain extraction technique using a template library," *Neuroimage*, vol. 55, no. 3, pp. 1091–1108, 2011.

[14] J. E. Iglesias, C.-Y. Liu, P. M. Thompson, and Z. Tu, "Robust brain extraction across datasets and comparison with publicly available methods," *IEEE Transactions on Medical Imaging*, vol. 30, no. 9, pp. 1617–1634, 2011.

[15] F. Segonne, A. Dale, E. Busa, M. Glessner, D. Salat, H. K. Hahn, and B. Fischl, "A hybrid approach to the skull stripping problem in MRI," *Neuroimage*, vol. 22, no. 3, pp. 1060–1075, 2004.

[16] R. Beare, J. Chen, C. L. Adamson, T. Silk, D. K. Thompson, J. Y. Yang, V. A. Anderson, M. L. Seal, and A. G. Wood, "Brain extraction using the watershed transform from markers," *Frontiers in neuroinformatics*, vol. 7, no. 32, 2013.

[17] D. E. Rex, D. W. Shattuck, R. P. Woods, K. L. Narr, E. Luders, K. Rehm, S. E. Stolzner, D. A. Rottenberg, and A. W. Toga, "A meta-algorithm for brain extraction in MRI," *NeuroImage*, vol. 23, no. 2, pp. 625–637, 2004.

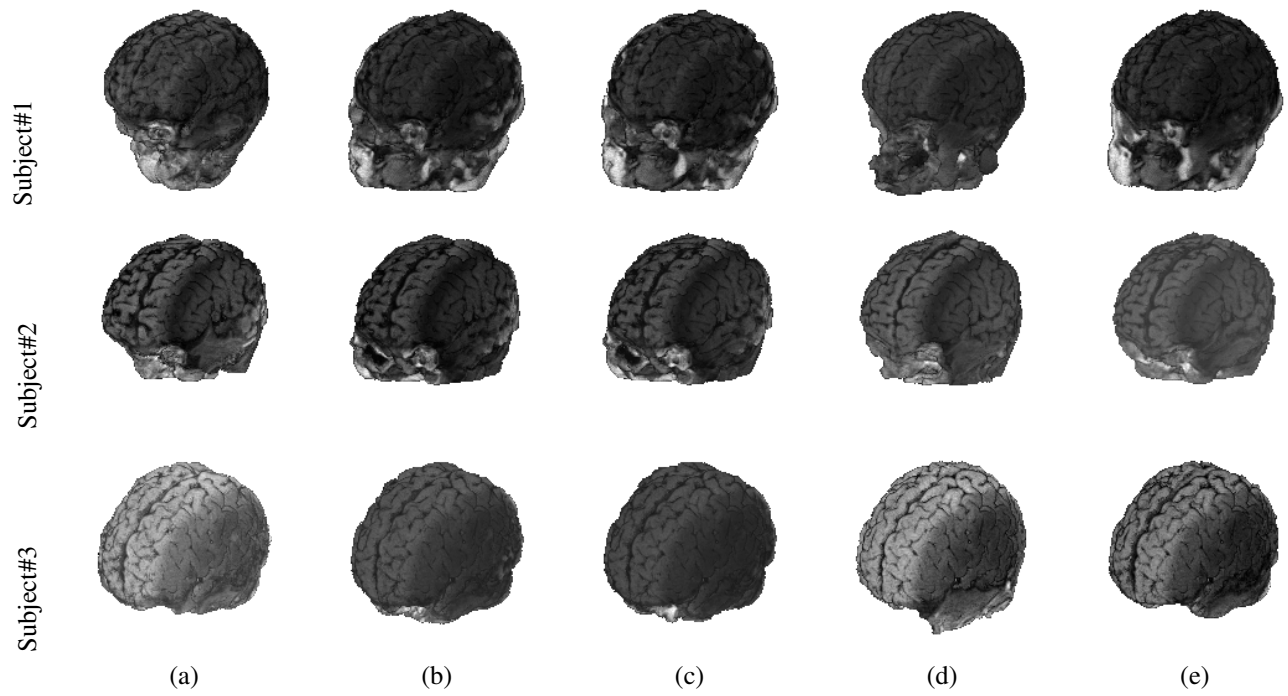

Fig. 13. 3D visualization of the segmented brain tissue for 3 different subjects using (a) our approach, (b) BET [4], (c) BET2 [40], (d) BSE [18], and (e) iBEAT [24].

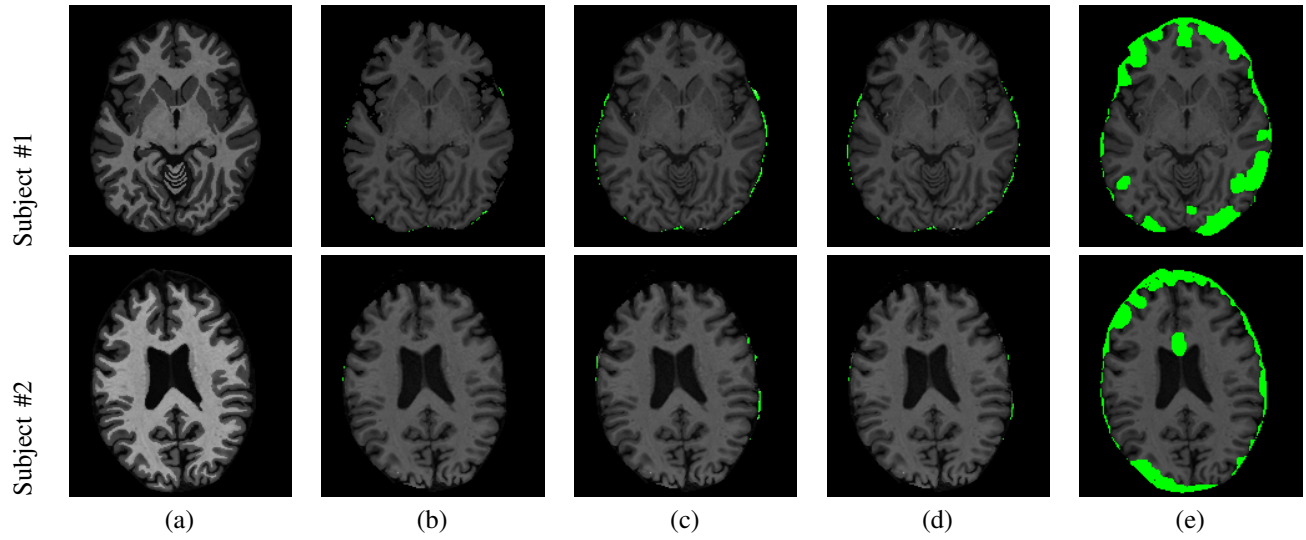

Fig. 14. Comparative brain extraction results for two independent adult subjects using (b) our approach, (c) BET [4], (d) BET2 [40], and (e) BSE [18]. Ground truth images are shown in (a). The BET factor used for BET and BET2 methods is the default value (0.5). Segmentation errors are highlighted in green. BET and BET2 did not discard all non-brain tissue, whereas BSE discarded non-brain, yet some parts of brain tissue were discarded as well.

TABLE I
COMPARATIVE ACCURACY OF OUR APPROACH VS. THE METHODS IN [4], [18], [24], [40] BY THE DSC, MHD, AND ABVD ON 30 INFANT DATA SETS WITH AVAILABLE GROUND TRUTH ("SD "– STANDARD DEVIATION).

	Evaluation Metric					
	DSC (%)		MHD (mm)		ABVD (%)	
Method	Mean±SD	*p*-value	Mean±SD	*p*-value	Mean±SD	*p*-value
OUR	96.77±1.45	——	4.14±1.76	——	4.95±2.62	——
iBEAT [24]	94.44±2.14	0.0162	9.31±8.96	0.04	7.27±1.92	0.0007
BET2 [40]	89.98±1.53	0.0001	11.03±7.4	0.0033	11.57±7.05	0.03
BET [4]	88.7±2.7	0.0001	13.6±5.6	0.0005	15.7±6.5	0.0001
BSE [18]	88.42±3.03	0.0001	18.4±4.02	0.0005	19.07±3.722	0.015

TABLE II
COMPARATIVE ACCURACY OF OUR APPROACH VS. THE METHODS IN [4], [18], [40] BY THE DSC, MHD, AND ABVD ON 18 ADULT DATA SETS WITH AVAILABLE GROUND TRUTH ("SD "– STANDARD DEVIATION).

	Evaluation Metric					
	DSC (%)		MHD (mm)		ABVD (%)	
Method	Mean±SD	p-value	Mean±SD	p-value	Mean±SD	p-value
OUR	93.11±2.4	——	8.43±1.88	——	6.7±1.13	——
BET2 [40]	92.60±2.86	0.0001	10.56±6.19	0.0001	7.42±7.67	0.2035
BET [4]	91.14±2.62	0.0001	11.26±5.83	0.0001	12.69±6.51	0.0001
BSE [18]	89.92±7.11	0.0026	15.12±10.09	0.0001	18.84±22.87	0.0001

[18] D. W. Shattuck and R. M. Leahy, "Brainsuite: an automated cortical surface identification tool," *Medical Image Analysis*, vol. 6, no. 2, pp. 129–142, 2002.

[19] B. D. Ward, "Intracranial segmentation," *Biophysics Research Institute, Medical College of Wisconsin, Milwaukee, WI*, 1999.

[20] A. M. Dale, B. Fischl, and M. I. Sereno, "Cortical surface-based analysis: I. Segmentation and surface reconstruction," *Neuroimage*, vol. 9, no. 2, pp. 179–194, 1999.

[21] J. Chiverton, K. Wells, E. Lewis, C. Chen, B. Podda, and D. Johnson, "Statistical morphological skull stripping of adult and infant MRI data," *Computers in biology and medicine*, vol. 37, no. 3, pp. 342–357, 2007.

[22] S. Kobashi, Y. Fujimoto, M. Ogawa, K. Ando, R. Ishikura, K. Kondo, S. Hirota, and Y. Hata, "Fuzzy-ASM Based Automated Skull Stripping Method from Infantile Brain MR Images," in *Granular Computing*, 2007, pp. 632–632.

[23] M. Pport, D. E. I. Ghita, E. Twomey, and P. F. Whelan, "A hybrid approach to brain extraction from premature infant MRI," in *Image Analysis*, 2011, pp. 719–730.

[24] F. Shi, L. Wang, Y. Dai, J. H. Gilmore, W. Lin, and D. Shen, "LABEL: Pediatric brain extraction using learning-based meta-algorithm," *NeuroImage*, vol. 62, no. 3, pp. 1975–1986, 2012.

[25] D. W. Shattuck, G. Prasad, M. Mirza, K. L. Narr, and A. W. Toga, "Online resource for validation of brain segmentation methods," *NeuroImage*, vol. 45, no. 2, pp. 431–439, 2009.

[26] C. Fennema-Notestine, I. B. Ozyurt, C. P. Clark, S. Morris, A. Bischoff-Grethe, M. W. Bondi, T. L. Jernigan, and G. G. Brown, "Quantitative evaluation of automated skull-stripping methods applied to contemporary and legacy images: Effects of diagnosis, bias correction, and slice location," *Human Brain Mapping*, vol. 27, no. 2, pp. 99–113, 2006.

[27] F. Shi, Y. Fan, S. Tang, J. H. Gilmore, W. Lin, and D. Shen, "Neonatal brain image segmentation in longitudinal MRI studies," *Neuroimage*, vol. 49, no. 1, pp. 391–400, 2010.

[28] A. U. Mewes, P. S. Hueppi, H. Als, F. J. Rybicki, T. E. Inder, G. B. McAnulty, R. V. Mulkern, R. L. Robertson, M. J. Rivkin, and S. K. Warfield, "Regional brain development in serial magnetic resonance imaging of low-risk preterm infants," *Pediatrics*, vol. 118, no. 1, pp. 23–33, 2006.

[29] M. Casanova, A. El-Baz, and J. Suri, "Imaging the brain in autism," in *Springer-Verlag, New York*, vol. ISBN-13, 2013.

[30] C. Bouman and K. Sauer, "A generalized gaussian image model for edge-preserving MAP estimation," *IEEE Transactions on Image Processing*, vol. 2, no. 3, pp. 296–310, 1993.

[31] N. J. Tustison, B. B. Avants, P. A. Cook, Y. Zheng, A. Egan, P. A. Yushkevich, and J. C. Gee, "N4ITK: improved N3 bias correction," *IEEE Transactions on Medical Imaging*, vol. 29, no. 6, pp. 1310–1320, 2010.

[32] J. Besag, "On the statistical analysis of dirty pictures," *Journal of the Royal Statistical Society. Series B (Methodological)*, pp. 259–302, 1986.

[33] D. Adalsteinsson, "A fast level set method for propagating interfaces," Ph.D. dissertation, Citeseer, 1994.

[34] A. El-Baz, A. Elnakib, F. Khalifa, M. A. El-Ghar, P. McClure, A. Soliman, and G. Gimelrfarb, "Precise segmentation of 3-D magnetic resonance angiography," *IEEE Transactions on Biomedical Engineering*, vol. 59, no. 7, pp. 2019–2029, 2012.

[35] A. Farag, A. El-Baz, and G. Gimel'farb, "Precise segmentation of multimodal images," *IEEE Transactions on Image Processing*, vol. 15, no. 4, pp. 952–968, 2006.

[36] A. El-Baz, "Novel stochastic models for medical image analysis," Ph.D. dissertation, University of Louisville, Louisville, KY, USA, 2006.

[37] D. Lee R, "Measures of the amount of ecologic association between species," *Ecology*, vol. 26, pp. 297–302, 1945.

[38] G. Gerig, M. Jomier, and M. Chakos, "Valmet: A new validation tool for assessing and improving 3D object segmentation," in *Medical Image Computing and Computer Assisted Intervention*, 2001, pp. 516–523.

[39] IBIS, "Infant brain imaging study," http://www.ibisnetwork.org/.

[40] M. Jenkinson, M. Pechaud, and S. Smith, "BET2: MR-based estimation of brain, skull and scalp surfaces," in *Eleventh Annual Meeting of The Organization for Human Brain Mapping*, vol. 17, 2005.